nature chemistry

ARTICLES

https://doi.org/10.1038/s41557-022-00926-z

Anisotropic dynamics of resonant scattering between a pair of cold aligned diatoms

Haowen Zhou, William E. Perreault, Nandini Mukherjee ✉ and Richard N. Zare ✉

The collision dynamics between a pair of aligned molecules in the presence of a partial-wave resonance provide the most sensitive probe of the long-range anisotropic forces important to chemical reactions. Here we control the collision temperature and geometry to probe the dynamics of cold (1–3 K) rotationally inelastic scattering of a pair of optically state-prepared D_2 molecules. The collision temperature is manipulated by combining the gating action of laser state preparation and detection with the velocity dispersion of the molecular beam. When the bond axes of both molecules are aligned parallel to the collision velocity, the scattering rate drops by a factor of 3.5 as collision energies >2.1 K are removed, suggesting a geometry-dependent resonance. Partial-wave analysis of the measured angular distribution supports a shape resonance within the centrifugal barrier of the $l = 2$ incoming orbital. Our experiment illustrates the strong anisotropy of the quadrupole–quadrupole interaction that controls the dynamics of resonant scattering.

Long-range molecular forces are a subject of intense interest because of their importance in initiating chemical reactions[1]. However, optical spectroscopy, which so effectively probes the deeply bound molecular states, cannot generally probe the most loosely bound states associated with the long-range part of the potential. As a result, its experimental interrogation remains challenging. Fortunately, low-energy scattering experiments are sensitive to weak, long-range molecular forces, but their small cross sections often cause experimental noise that masks important detail. Dynamic resonances, which represent positive energy quasi-bound states of the collision complex, enhance the scattering probability in this interaction range. Several crossed-beam and merged-beam techniques have demonstrated the ability to tune the collision energy in the low-energy regime and capture the increase in cross section that accompanies a scattering resonance. Both orbiting[2–8] and Feshbach[9] resonances were detected using various collision pairs. While these remarkable experiments were able to detect scattering resonances, they provided only limited direct information on the dynamics of the resonant collision complex.

Recently, a few experimental studies have begun to illustrate the dynamics of a scattering resonance by simultaneously measuring the scattering angular distribution[10–15]. In the presence of a resonance, the scattering is dominated by a single incoming orbital or partial wave that produces a finite number of scattered orbitals. The interference of the limited number of outgoing orbitals generates a characteristic structure in the scattering angular distribution that can be used as a fingerprint of the resonance[11,16,17]. The quasi-bound states, which are formed within the centrifugal barrier of the orbital angular momentum, depend sensitively on the long-range van der Waals interactions[2]. However, the ability of these measurements to interrogate the potential is limited by any averaging over internal molecular quantum states. To understand completely how each orbital is scattered by the interaction potential as energy is exchanged between different degrees of freedom, it is essential to eliminate averaging by fully defining the internal energy states in the incoming and outgoing channels.

However, even controlling the temperature and internal energy is insufficient to map the inherently anisotropic electrostatic force fields that drive molecular processes. To fully explore the rich dynamics of diatom–diatom interactions experimentally, we must also control the collision geometry[18], which requires the selection of the m state distribution within a single rovibrational energy level for each partner[19]. A large number of theoretical studies have illustrated in great detail the importance of the relative alignment of the colliding pair on the dynamics of cold diatom–diatom scattering[19–27]. Unfortunately, the vast majority of experimental work thus far has not explored the effect of the spatial alignment of the collision partners on the scattering process, and so there are almost no data available for comparison with theory. Defining the initial state with this level of precision is equivalent to setting the boundary conditions for experimentally solving the dynamic equations. A scattering experiment probing the dynamic resonance with complete control of both the internal and external degrees of freedom will provide invaluable data elucidating the long-range anisotropic forces so important to chemistry. Completely alignment-controlled diatom–diatom scattering experiments have been greatly anticipated by theoreticians and experimentalists alike and might be considered one of the holy grails of scattering studies.

We previously conducted a series of quantum-state-controlled cold-scattering experiments that made substantial progress toward the goal of complete control[28–30]. These experiments used control over molecular alignment to demonstrate remarkable stereodynamic effects, which probably resulted from dynamic resonances. However, in these experiments the presence of a scattering resonance was only speculated, not directly proven, because the collision energy was not tuned. Additionally, we have previously only been able to control the alignment of one of the partner molecules, partially obscuring the effects of the anisotropic collision forces on the scattering dynamics.

In this article we report a quantum-controlled collision experiment that probes resonance dynamics by manipulating the molecular alignment with respect to the collision velocity and to the collision energy. In these experiments we prepared D_2 molecules in a rovibrationally excited, aligned quantum state ($v = 2$, $j = 2$, m), and studied the $\Delta j = 2$ rotational relaxation D_2 ($v = 2$, $j = 2$, m) → ($v = 2$, $j' = 0$) within a supersonically expanded pure beam of D_2 molecules.

Department of Chemistry, Stanford University, Stanford, CA, USA. ✉e-mail: nmukherj@stanford.edu; zare@stanford.edu

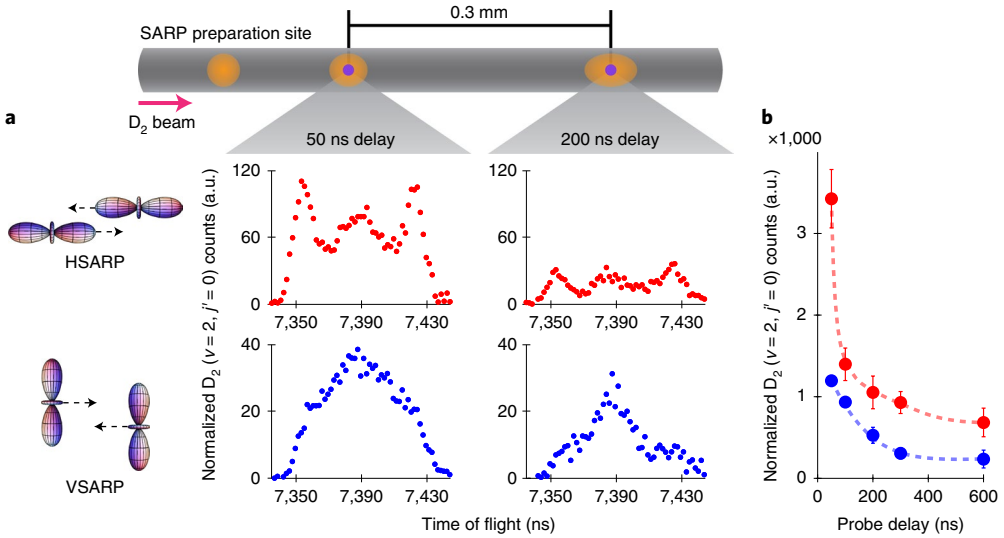

Fig. 1 | HSARP and VSARP scattering rates as the probe beam moves along the molecular beam propagation direction. a, Top: schematic showing the SARP preparation of the molecular beam (orange spot, ~100 μm). As the delay is increased, this spot propagates downstream and spreads along the propagation direction. As described in the text, only those scattering products within the small REMPI probe volume (purple spots, ~20 μm) are detected. Bottom: graphs showing the measured time-of-flight distributions of scattered D_2 ($v=2, j'=0$) for the HSARP (red dots) and VSARP (blue dots) alignments at delays of 50 and 200 ns following SARP preparation. In HSARP, the total number of counts drops by a factor of ~3.5, while for VSARP it drops by a factor of ~2 as the delay is increased from 50 to 200 ns. **b**, Relative HSARP and VSARP integral scattering rates as a function of SARP-REMPI delay in nanoseconds. The HSARP scattering rate drops dramatically as the delay is increased from 50 to 600 ns, while the VSARP rate drops much more mildly, indicating the presence of a geometry-dependent collisional resonance. The dashed lines are only visual guides. Error bars, 1 s.d. All data presented here were normalized with respect to the REMPI power.

Here, v and j give the vibrational and rotational quantum numbers, respectively, while m gives the projection of the internal angular momentum on a chosen quantization axis. The state preparation of the D_2 molecules combined with probing using nanosecond laser pulses provides a gating action that can be used to effectively reduce the longitudinal beam temperature for the state-prepared molecules. We show that the width of the velocity distribution of the aligned molecules contributing to the collision process is decreased by increasing the delay between the preparation and probe lasers, which reduces the available collision energy by removing hotter collisions. This is similar in principle to the evaporative cooling used to achieve Bose–Einstein condensation of atomic gases[31]. The strong nonlinear response of the scattering rate to changes in the collision energy indicates that the scattering is dominated by a resonance involving a pair of rotationally aligned D_2 ($v=2, j=2$) molecules. Partial-wave analysis of the measured angular distributions suggests that the dynamic resonance is formed within the centrifugal barrier of the incoming partial wave with angular momentum $l=2$. Based on our analysis, we conclude that the long-range quadrupole–quadrupole interaction between a pair of rotating molecules contributes strongly to this dynamic resonance.

By aligning the bond axes of both colliding partner molecules either parallel or perpendicular to the approach direction, we fully define the geometry of a diatom–diatom collision. We show that the resonant dynamics sensitively depend on the collision geometry, revealing the strongly anisotropic character of the molecular forces involved. The anisotropy in the quadrupole–quadrupole interactions we report here parallels earlier measurements on the dipole–dipole scattering between two electric-field-oriented ultracold KRb molecules[32], which demonstrated dramatic changes in the reaction barrier for the head-to-tail versus side-on orientations.

Results

We study collisions in the cold, controlled environment of a collimated supersonic molecular beam, which defines the collision velocity direction in the lab frame. To study the $\Delta j=2$ rotational relaxation, nearly the complete (>95%) D_2 ($v=0, j=0$) population in this beam is pumped into the rovibrationally excited D_2 ($v=2$, $j=2$) state using Stark-induced adiabatic Raman passage (SARP)[33]. SARP prepares the quantum state using a pair of partially overlapping nanosecond laser pulses[34–36], and controls the bond axis alignment by selecting specific m states within the rovibrational (v, j) eigenstate[37]. Two specific bond axis alignments, referred to as HSARP and VSARP, were prepared using appropriately polarized laser pulses[28]. In HSARP the bond axis of D_2 ($v=2, j=2$) is preferentially aligned along the collision velocity, while for the VSARP state the bond axis is aligned perpendicularly. The bond axes are prepared with respect to the well-defined collision velocity axis, thereby controlling the collision geometry at the molecular level.

The rotational relaxation of the prepared D_2 ($v=2, j=2$) in the pure D_2 beam can be mediated by either another state-prepared D_2 ($v=2, j=2$), or an unprepared D_2 ($v=0, j=1, 2$) in the ground vibrational level. The $\Delta j=2$ rotationally relaxed D_2 ($v=2, j'=0$) scattering product is detected by (2 + 1) resonance-enhanced multiphoton ionization (REMPI). The scattering signal is maximized when the REMPI spot is centred on the moving volume of SARP molecules (Fig. 1). This is because the rotationally relaxed D_2 ($v=2, j'=0$) molecules, which move at ~800 m s^{-1} with respect to the molecular beam frame, are rapidly deflected out of the beam after they are produced. As a result, only those collisions that occur within the REMPI volume are detected.

The scattered molecules were detected at five different REMPI probe delays ranging from 50 to 600 ns following SARP preparation. This range of probe delays corresponds to probe distances of 0.1–1.2 mm downstream from the SARP preparation site along the molecular beam, which is much greater than the probe spot size of ~20 μm. Figure 1a shows the measured time-of-flight distributions of the rotationally relaxed D_2 ($v=2, j'=0$) for the HSARP and VSARP alignments measured at probe delays of 50 and 200 ns. Immediately, we see that the scattering rate drops dramatically

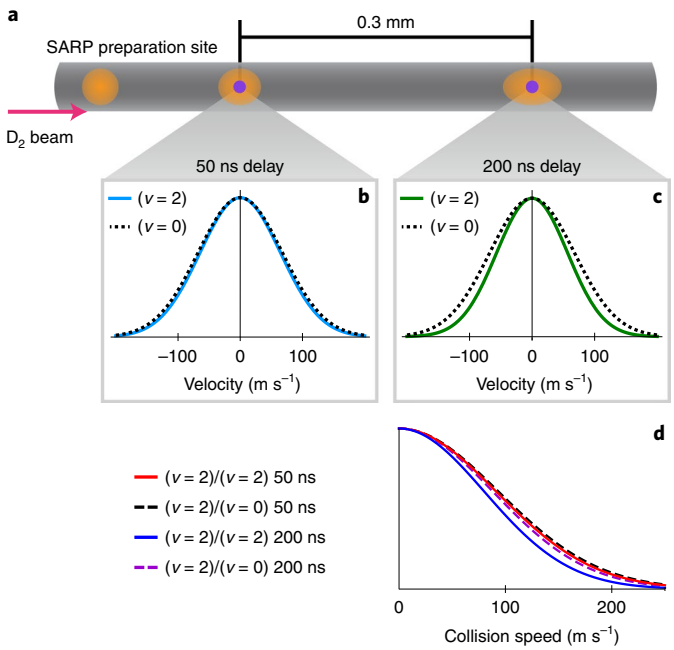

Fig. 2 | Velocity distribution measured within the probe volume as the probe is moved along the direction of molecular beam propagation. All velocities are determined by fitting the time-of-flight distribution (see Supplementary Information, section 1), which gives a measurement error of less than ±2 m s^{-1}. **a**, Schematic showing the SARP preparation of the molecular beam (orange spot, ~100 µm). As the delay is increased, this spot propagates downstream and spreads along the propagation direction. As described in the text, only those scattering products within the small REMPI probe volume (purple spots, ~20 µm) are detected. **b**, The velocity distributions of SARP-prepared D_2 ($v=2$, $j=2$) (cyan curve) and unprepared D_2 ($v=0$, $j=1$, 2) (black dotted curve) at 50 ns delay. **c**, The velocity distributions of the prepared D_2 ($v=2$, $j=2$) (green curve) and unprepared D_2 ($v=0$, $j=1$, 2) (black dotted curve) at 200 ns delay. **d**, Collision speeds for both the aligned–aligned (red and blue solid curves) and aligned–unaligned (black and purple dashed curves) collision pairs at the two delays. These curves are generated by convoluting the velocity distributions shown in **b** and **c**. See Methods and Supplementary Information, section 2 for details. The only substantial change is in the collision speed for the aligned–aligned collisions at 200 ns (solid blue curve). All three other curves fall within our measurement error.

for the HSARP alignment when the delay is increased from 50 to 200 ns, while it drops much more mildly for the VSARP alignment. Figure 1b shows the HSARP and VSARP integral scattering rates as a function of the probe delay from 50 to 600 ns. The figure shows that most of the change in the HSARP and VSARP scattering rates occurs as the probe delay increases from 50 to 200 ns. We verified experimentally that the molecular beam intensity remained constant over this range.

To understand the strong nonlinear variation of the scattering rate in response to the changes in probe delay (Fig. 1), we examined the collision velocity distribution at the different delays. To that end, the velocity distributions of both the prepared and unprepared D_2 molecules were measured using time-of-flight mass spectrometry following (2+1) REMPI at each delay (Supplementary Information, section 1). We find that for the SARP-prepared D_2 ($v=2$, $j=2$) the $1/e$ width of the distribution reduces from 92 ± 1 m s^{-1} to 67 ± 2 m s^{-1} as the probe delay is increased from 50 to 600 ns, while for the unprepared D_2 ($v=0$) it remains constant at 96 ± 1 m s^{-1}. Figure 2b,c shows the velocity distributions of both SARP-prepared and unprepared D_2 molecules at two different locations along the molecular beam corresponding to probe delays of 50 and 200 ns following the SARP preparation. The solid curves show that the velocity distribution of the SARP-prepared D_2 ($v=2$) is squeezed along the direction of beam propagation. Because it is the only change that we measure, the reduction in the longitudinal beam temperature must correlate with the dramatic change in scattering rate shown in Fig. 1.

To understand this velocity-narrowing effect, we must consider the fact that both SARP preparation and REMPI detection take place within the narrow confines of the focused laser spots on the molecular beam and have interaction times of only a few nanoseconds. By transferring all the ground-state D_2 ($v=0$, $j=0$) molecules to the ($v=2$, $j=2$) state within its ~100 µm laser spot irrespective of their velocities, SARP sets a time $t=0$ for the state-prepared D_2 ($v=2$, $j=2$) molecules (orange spots in the schematics of Figs. 1a and 2a). Afterwards, the state-prepared D_2 with different velocities will disperse in space along the molecular beam propagation direction as shown by the elongation of the orange spots in the schematics in Figs. 1 and 2 as the delay is increased. Detection by the REMPI laser (~20 µm, 5 ns), which is shown by the purple spot in the schematics, acts like a temporal gate that sets a narrow time window for the SARP-prepared D_2 molecules to arrive at the probe location. As the molecules travel further from the preparation site, the D_2 ($v=2$, $j=2$) molecules that have the largest deviations from the mean beam velocity move out of the small probe volume. Because of the gating action that results from the combined operation of SARP preparation and REMPI detection, an increasingly narrow velocity group is selected as the detection location is moved farther away from the SARP preparation site. The effect of the gating is demonstrated by the contrast between the two solid curves in Fig. 2b,c.

The hottest collisions occur between molecules in the opposite tails of the velocity distributions, and so the available collision energy will be reduced for aligned–aligned collisions as the width of the distribution reduces with increasing delay. This is analogous to the evaporative cooling of atomic gases by removing hot atoms from an optical dipole trap. The narrowing can be quantified in terms of u_{90}, which we define as the upper bound of the collision speed range that contains 90% of the aligned–aligned collisions at a given delay. We have calculated the value of u_{90} from the collision speed distributions measured for each probe delay (Supplementary

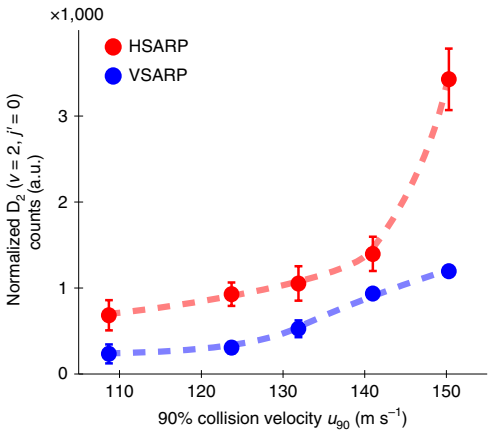

Fig. 3 | HSARP (red dots) and VSARP (blue dots) relative integral scattering rates as a function of the collision speed u_{90} (m s^{-1}). The collision speed u_{90} is defined as the upper bound of the collision speed range that contains 90% of the collisions at that delay, that is, $u_c \leq u_{90}$ for 90% of collisions. As the delay is changed from 50 to 600 ns, the value of u_{90} changes from 150 to 109 m s^{-1}. The nonlinear dependence of the scattering rates on the collision speed indicates the presence of a collisional resonance. The dashed lines are only visual guides. Error bars, 1 s.d.

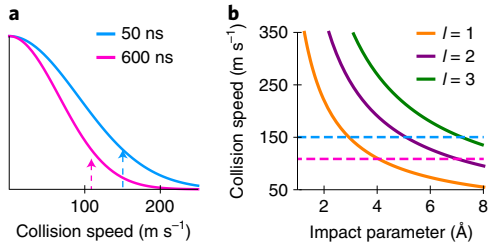

Fig. 4 | Incoming orbitals *l* contributing to the $\Delta j = 2$ inelastic scattering. **a**, The collision speed distribution for the D_2 ($v=2$)/D_2 ($v=2$) collision pair at 50 ns (solid cyan) and 600 ns delay (solid magenta). The vertical cyan and magenta dashed lines mark the upper bound of collision velocity (u_{90}) containing 90% of the D_2 ($v=2$)/ D_2 ($v=2$) collisions at 50 and 600 ns delays, respectively. **b**, Contour lines for the orbital angular momenta $l=1$ (solid orange), $l=2$ (solid purple) and $l=3$ (solid green) as a function of the collision speed (u_c) and impact parameter (b). These curves were calculated using the semiclassical expression $u_c = \sqrt{l(l+1)}\,\hbar/\mu b$, where μ is the reduced mass. The cyan and magenta horizontal dashed lines display the value of u_{90} for the delays of 50 and 600 ns corresponding to the vertical dashed lines in **a**. The crossing point of the u_{90} lines with the contours for the various orbitals determines the minimum value of the impact parameter. For a partial wave to contribute to the collision process, this minimum value must be within the range of the scattering potential.

Table 2). We find that at 50 ns delay $u_{90} = 150\,\mathrm{m\,s^{-1}}$, whereas at 600 ns $u_{90} = 109\,\mathrm{m\,s^{-1}}$. Equivalently, at 50 ns delay 90% of collisions occur with collision energy $\leq$2.7 K, whereas at 600 ns delay the upper bound reduces to 1.4 K, corresponding to an average change in temperature of ~0.25 K per 100 ns delay. We describe the tuning action of our method in terms of the differential change in u_{90} rather than the mean speed because it relies on removing the most extreme collisions with each successive increase in the delay. This is very different from most established methods, which tune collision energy by changing the mean of a narrow distribution.

In Fig. 2d, we compare the collision speed distributions for both the aligned–aligned and aligned–unaligned collision pairs at 50 and 200 ns delay, calculated by convoluting the measured distributions of the individual partners as described in the Methods and in Supplementary Information, section 2. Hot collisions between the state-prepared D_2 ($v=2$) molecules are removed as the probe delay is increased further, which creates the visible reduction in the aligned–aligned collision speed distribution seen in Fig. 2d at 200 ns probe delay. For the unprepared D_2 there is nothing that sets a time $t=0$, and so its velocity spectrum remains unchanged with delay and distance as shown by the dotted curves in Fig. 2b,c. As a result, the collision temperature does not significantly change for the aligned–unaligned collisions with increasing delay.

The change in aligned–aligned collision speed correlates with the drastic reduction in scattering rate as a function of delay shown in Fig. 1b. Because the measured differential and integral scattering rates in Fig. 1 originate only from the SARP-prepared D_2 molecules found within the small REMPI volume at the time of probing, we conclude that the changes in the observed scattering rates for both alignments result from the reduction of the aligned–aligned collision speed or temperature as a function of probe delay. The correlation between the scattering rate and the collision speed clearly suggests that the observed rotational relaxation of D_2 ($v=2, j=2$) is caused via collision with another D_2 ($v=2, j=2$). We use conservation of energy to confirm that only one of the D_2 molecules in the aligned–aligned scattering pair is rotationally relaxed during the collision event. Because we do not select the nuclear spin state of the SARP-prepared D_2 molecules, only one-sixth of the aligned–aligned scattering involves a pair of identical bosons.

Figure 3 shows the relative integral scattering rates for the HSARP and VSARP alignments as a function of the collision speed u_{90}. The scattering rate is defined as the product of cross section and the collision speed. Previous theoretical studies of the H_2–H_2 collision system have shown that in the absence of resonance the collision cross section changes very slowly in this temperature range[22,23,38]. In the absence of a collisional resonance, the scattering rate should exhibit nearly linear behaviour as the collision speed is varied. The nonlinear behaviour shown in Fig. 3 is thus very strong evidence for the presence of a scattering resonance for the aligned–aligned $\Delta j=2$ rotationally inelastic scattering. While differential tuning of collision speed implies the presence of a quasi-resonant state for the $\Delta j=2$ scattering, it fails to identify the resonant partial wave. Our partial-wave analysis shows that the scattering process is dominated by the $l=2$ incoming orbital which is fingerprinted in the differential scattering angular distribution.

Discussion

Fundamental scattering theory allows us to express the scattering angular distribution as a coherent sum of the outgoing or scattered orbitals, the angular wavefunctions of which are given by the spherical harmonics $Y_{l',m_{l'}}(\theta,\varphi)$ (refs. [39,40]). As discussed in our earlier work[28–30], the scattering angular distributions can be fitted using these expressions to determine the outgoing orbitals produced by the collision process. The outgoing orbitals (l', $m_{l'}$) that need to be considered in these fits are those that can be generated by the scattering of all the incoming orbitals (l,m_l). For our cold collisions, only incoming orbitals with angular momentum $l=0$–2 will have impact parameters less than the ~7 Å range of the scattering potential[41] as shown by Fig. 4, which gives the semiclassical orbital angular momentum contours as a function of the collision speed and impact parameter. The orbital angular momentum couples with the internal angular momentum of the molecules to produce the total angular momentum, which must be conserved throughout the collision. From this conservation principle, we determine that only outgoing waves $l'=0$–6 need to be considered in our fits of the scattering angular distribution. Using this set of outgoing partial waves, we performed a partial-wave fitting of the measured angular distribution of the scattered D_2 ($v=2$, $j'=0$) for the HSARP and VSARP alignments at 50 ns delay, the results of which are shown in Fig. 5. Details on the partial-wave fitting procedure can be found in Supplementary Information, section 3.

Figure 5 shows that only the even outgoing orbitals $l'=0$, 2, 4, 6 produce good fits of the HSARP and VSARP angular distributions (solid curves), yielding $R^2>0.99$ for both HSARP and VSARP fits. In contrast, the odd outgoing orbitals $l'=1$, 3, 5 are not able to fit the data as shown by the dashed curve in Fig. 5a. As described below, the quadrupolar interactions responsible for the $\Delta j=2$ transition lead to the selection rule $\Delta l=0, \pm2, \pm4$ for the orbitals. As a result, the parity is conserved in the scattering process, meaning that even outgoing orbitals arise selectively from the scattering of even incoming orbitals. Therefore, the fact that the scattering distributions can be fitted with exclusively the even outgoing orbitals $l'=0$, 2, 4, 6 suggests that only the even incoming orbitals $l=0$, 2 contribute to the cold scattering. In contrast, the failure to fit the angular distributions with the odd outgoing orbitals $l'=1$, 3, 5 indicates a negligible contribution from the incoming orbital $l=1$. According to an earlier theoretical calculation on HD–H_2 scattering[38], the $l=1$ resonant complex represents a bound state below the HD–H_2 dissociation limit, and therefore it is not accessible by the colliding pair, which agrees with the result of our partial-wave analysis. Further, the excellent fit to the measured angular distributions, which assumes no reorientation of the partner molecule, confirms that the partner behaves as a spectator that provides the highly anisotropic force field responsible for the rotational relaxation.

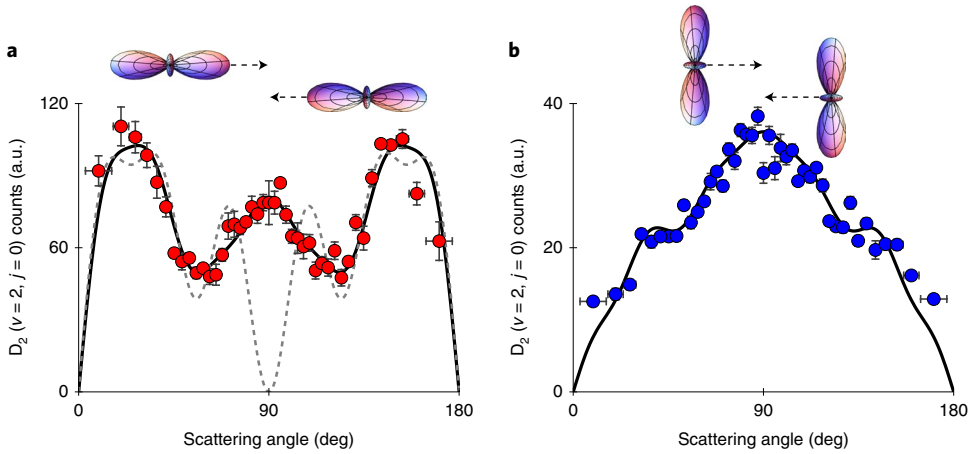

Fig. 5 | Partial-wave fitting of the measured scattering angular distribution. a,**b**, Experimentally measured scattering angular distributions and fits using partial-wave analysis for HSARP **(a)** and VSARP **(b)** bond-axis alignments. The red and blue dots represent the HSARP and VSARP experimental data taken at 50 ns delay, respectively. The solid and dashed black curves in **a** represent fits with even ($l' = 0, 2, 4, 6$) and odd ($l' = 1, 3, 5$) outgoing orbitals, respectively. Clearly the odd orbitals fail to generate a reasonable fit for the scattering distribution. Both HSARP and VSARP can be fitted well ($R^2 > 0.99$) using only even outgoing orbitals, generating a set of self-consistent fitting parameters as described in Supplementary Information, section 3. The vertical error bars represent 1 s.d. in each time-of-flight bin, and the horizontal error bars represent the experimental uncertainty in the angle determination.

In Table 1 we present the relative amplitudes of the even outgoing orbitals determined from the fit of the HSARP data. Additionally, we show how the various outgoing orbitals are generated from the scattering of incoming orbitals by the two leading quadrupolar terms of the expanded interaction potential $U_{202}(r)\, Y_{2m}(\theta_1, \varphi_1)\, Y_{00}(\theta_2, \varphi_2)\, Y^*_{2m}(\theta, \varphi)$ and $U_{224}(r)\, Y_{2m_1}(\theta_1, \varphi_1)\, Y_{2m_2}(\theta_2, \varphi_2)\, Y^*_{4(m_1+m_2)}(\theta, \varphi)$ (refs. [20,42,43]). Here, (θ_1, φ_1) and (θ_2, φ_2) define the alignments of the interacting diatoms in the centre-of-mass frame, and (r, θ, φ) defines the radial vector **r** connecting the centre-of-mass of the two molecules. The potential term U_{202} represents the anisotropic interaction that leaves the rotational state of the partner unchanged and is therefore similar to the anisotropy that drives $\Delta j = 2$ transitions in atom–diatom collisions. The quadrupole–quadrupole interactions where both molecular rotations are coupled result exclusively from U_{224}, which has the largest long-range contribution.

A scattering resonance is identified when the outgoing orbitals correlate dominantly to a single incoming orbital[6,8,17,44]. Table 1 shows that the outgoing orbital $l' = 0$ has the largest amplitude, and arises exclusively from the scattering of the input orbital $l = 2$ by the anisotropic interaction U_{202}. We note that the outgoing $l' = 6$ orbital is generated exclusively from the scattering of the incoming $l = 2$ orbital by the long-range quadrupole–quadrupole interaction U_{224}. In contrast, the scattered orbitals $l' = 2, 4$ include contributions from both $l = 0$ and 2 via the long-range interactions U_{202} and U_{224}. Table 1 shows that the scattered orbitals dominantly correlate to the incoming $l = 2$ or d-wave that faces a centrifugal barrier to low-energy scattering. The strong scattering of the d-wave indicates excitation of a quasi-resonant D_2–D_2 collision complex contained within the centrifugal barrier of the $l = 2$ orbital. This quasi-resonant state becomes accessible at higher collision energies that are available at short delays close to the SARP preparation site. With increasing delay, the required impact parameter for the resonant $l = 2$ orbital increases. In fact, Fig. 4 shows that the $l = 2$ impact parameter at 600 ns delay falls at the very edge of the interaction range[41], qualitatively explaining the dramatic decrease in collision rate.

Table 1 | Amplitudes of outgoing orbitals, correlated incoming orbitals and associated potential terms that connect the two determined from our even wave fit of the HSARP angular distribution as described in the text and shown in Fig. 5a

Outgoing orbital $Y_{l',m_{l'}}(\theta, \varphi)$	Amplitude of outgoing orbital $c_{l',m_{l'}}$	Correlating incoming orbital l
Y_{00}	1	$l = 2$ via U_{202}
Y_{20}	0.27	$l = 0$ via U_{202}, $l = 2$ via U_{202} and U_{224}
Y_{40}	0.21 exp [i 0.7]	$l = 0$ via U_{224}, $l = 2$ via U_{202} and U_{224}
Y_{60}	0.24 exp [i 1.7]	$l = 2$ via U_{224}

Because the HSARP and VSARP scattering angular distributions are generated by the same set of scattering matrix elements, the fits shown in Fig. 5 have been constrained to generate a self-consistent set of expansion coefficients $c_{l',m_{l'}}$. As such, there is no additional information about the scattering resonance contained in the VSARP coefficients. The complete set of scattering coefficients and their uncertainties are given in Supplementary Tables 2, 4 and 5.

Conclusions

We have combined control over the molecular alignment using SARP with a new method of collision energy tuning in our study of the rotational relaxation D_2 ($v = 2$, $j = 2$) → D_2 ($v' = 2$, $j' = 0$) in a pure beam of D_2. The state preparation of the molecules using SARP combined with REMPI probing using nanosecond laser pulses at a downstream point along the molecular beam, provides a gating action that effectively narrows the longitudinal velocity distribution as the delay between preparation and detection is increased. With the removal of the wings of the velocity distribution at larger delays, the hotter collisions are eliminated, enabling differential control of the collision energy. This laser gating mechanism selectively controls the collision speed of only the state-prepared molecules, allowing us to observe specifically the dynamics of a collision process between state-prepared partners. Further, because we measure scattering between two state-prepared molecules, the polarization directions of the SARP laser fields can align both partners either parallel (HSARP) or perpendicular (VSARP) to the approach direction, thus fully controlling the collision geometry at the molecular level.

By combining collision energy tuning with partial-wave analysis of the scattering angular distribution, our study provides strong evidence for a collision-geometry-dependent $l = 2$ shape resonance in the aligned–aligned D_2 ($v = 2$, $j = 2$) $\Delta j = 2$ rotational relaxation. We observe remarkably different angular distributions and responses of

the scattering rates to changes in the collision energy for the HSARP and VSARP preparations, thus demonstrating that low-temperature scattering is extremely sensitive to the collision geometry. We interpret the strong nonlinear behaviour of scattering rate observed for the HSARP geometry in response to the change in collision speed as the delay is increased from 50 to 200 ns to indicate the presence of a dynamic resonance that is accessible to the hot collisions more prevalent at 50 ns. The VSARP scattering rate reduces much less dramatically as the collision temperature is decreased. Thus, we believe our experiment demonstrates how sensitively the resonance behaviour depends on the collision geometry for this diatom–diatom scattering system. This illustrates the strong anisotropy of the long-range quadrupole–quadrupole interaction that controls the resonant dynamics, suggesting that these anisotropic effects will probably be present in other diatom–diatom collisions. The aligned–aligned scattering reported here is among the first of its kind, approaching the experimental ideal of complete control over both the internal and external degrees of freedom. The nearly complete control that we have achieved here breaks new ground in the understanding of the geometric dependence of scattering dynamics, which has important implications in cold and ultracold four-centre collision processes[45].

Online content

Any methods, additional references, Nature Research reporting summaries, source data, extended data, supplementary information, acknowledgements, peer review information; details of author contributions and competing interests; and statements of data and code availability are available at https://doi.org/10.1038/s41557-022-00926-z.

Received: 23 March 2021; Accepted: 9 March 2022;
Published online: 02 May 2022

References

1. Weck, P. F. & Balakrishnan, N. Importance of long-range interactions in chemical reactions at cold and ultracold temperatures. *Int. Rev. Phys. Chem.* **25**, 283–311 (2006).
2. Naulin, C. & Costes, M. Experimental search for scattering resonances in near cold molecular collisions. *Int. Rev. Phys. Chem.* **33**, 427–446 (2014).
3. Henson, A. B., Gersten, S., Shagam, Y., Narevicius, J. & Narevicius, E. Observation of resonances in Penning ionization reactions at sub-kelvin temperatures in merged beams. *Science* **338**, 234–239 (2012).
4. García-Vela, A., Cabanillas-Vidosa, I., Ferrero, J. C. & Pino, G. A. The role of orbiting resonances in the vibrational relaxation of I_2 (B,$v'=21$) by collisions with He at very low energies: a theoretical and experimental study. *Phys. Chem. Chem. Phys.* **14**, 5570 (2012).
5. Lavert-Ofir, E. et al. Observation of the isotope effect in sub-kelvin reactions. *Nat. Chem.* **6**, 332–335 (2014).
6. Bergeat, A., Onvlee, J., Naulin, C., Van Der Avoird, A. & Costes, M. Quantum dynamical resonances in low-energy CO($j=0$) + He inelastic collisions. *Nat. Chem.* **7**, 349–353 (2015).
7. Jankunas, J., Jachymski, K., Hapka, M. & Osterwalder, A. Observation of orbiting resonances in He ($^3S_1$) + NH_3 Penning ionization. *J. Chem. Phys.* **142**, 164305 (2015).
8. Costes, M. & Naulin, C. Observation of quantum dynamical resonances in near cold inelastic collisions of astrophysical molecules. *Chem. Sci.* **7**, 2462–2469 (2016).
9. Köhler, T., Góral, K. & Julienne, P. S. Production of cold molecules via magnetically tunable Feshbach resonances. *Rev. Mod. Phys.* **78**, 1311–1361 (2006).
10. Wang, T. et al. Dynamical resonances accessible only by reagent vibrational excitation in the F + HD → HF + D reaction. *Science* **342**, 1499–1502 (2013).
11. Vogels, S. N. et al. Imaging resonances in low-energy NO–He inelastic collisions. *Science* **350**, 787–790 (2015).
12. Yang, T. et al. Extremely short-lived reaction resonances in Cl + HD ($v=1$) → DCl + H due to chemical bond softening. *Science* **347**, 60–63 (2015).
13. Onvlee, J. et al. Imaging quantum stereodynamics through Fraunhofer scattering of NO radicals with rare-gas atoms. *Nat. Chem.* **9**, 226–233 (2016).
14. Vogels, S. N. et al. Scattering resonances in bimolecular collisions between NO radicals and H_2 challenge the theoretical gold standard. *Nat. Chem.* **10**, 435–440 (2018).
15. Paliwal, P. et al. Determining the nature of quantum resonances by probing elastic and reactive scattering in cold collisions. *Nat. Chem.* **13**, 94–98 (2021).
16. Klein, A. et al. Directly probing anisotropy in atom–molecule collisions through quantum scattering resonances. *Nat. Phys.* **13**, 35–38 (2017).
17. de Jongh, T. et al. Imaging the onset of the resonance regime in low-energy NO–He collisions. *Science* **368**, 626–630 (2020).
18. Aoiz, F. J. et al. A new perspective: imaging the stereochemistry of molecular collisions. *Phys. Chem. Chem. Phys.* **17**, 30210–30228 (2015).
19. Schaefer, J. & Meyer, W. Theoretical studies of H_2–H_2 collisions. I. Elastic scattering of ground state *para*- and *ortho*-H_2 in the rigid rotor approximation. *J. Chem. Phys.* **70**, 344–360 (1979).
20. Buck, U., Huisken, F., Maneke, G. & Schaefer, J. State resolved rotational excitation in HD + D_2 collisions. I. Angular dependence of 0 → 2 transitions. *J. Chem. Phys.* **74**, 535–544 (1981).
21. Lee, T.-G. et al. State-to-state rotational transitions in H_2 + H_2 collisions at low temperatures. *J. Chem. Phys.* **125**, 114302 (2006).
22. Quéméner, G. & Balakrishnan, N. Quantum calculations of H_2–H_2 collisions: from ultracold to thermal energies. *J. Chem. Phys.* **130**, 11430 (2009).
23. Balakrishnan, N., Quéméner, G., Forrey, R. C., Hinde, R. J. & Stancil, P. C. Full-dimensional quantum dynamics calculations of H_2–H_2 collisions. *J. Chem. Phys.* **134**, 014301 (2011).
24. Sultanov, R. A., Guster, D. & Adhikari, S. K. Low temperature HD + *ortho*-/*para*-H_2 inelastic scattering of astrophysical interest. *J. Phys. B* **49**, 015203 (2016).
25. Jambrina, P. G. et al. Stereodynamical control of a quantum scattering resonance in cold molecular collisions. *Phys. Rev. Lett.* **123**, 43401 (2019).
26. Croft, J. F. E. & Balakrishnan, N. Controlling rotational quenching rates in cold molecular collisions. *J. Chem. Phys.* **150**, 044116 (2019).
27. Yang, B. et al. Quantum dynamics of CO–H_2 in full dimensionality. *Nat. Commun.* **6**, 6629 (2015).
28. Perreault, W. E., Mukherjee, N. & Zare, R. N. Quantum control of molecular collisions at 1 kelvin. *Science* **358**, 356–359 (2017).
29. Perreault, W. E., Mukherjee, N. & Zare, R. N. Quantum controlled rotationally inelastic scattering of HD with H_2 and D_2 near 1 kelvin reveals collisional partner reorientation. *Nat. Chem.* **10**, 561–567 (2018).
30. Perreault, W. E., Mukherjee, N. & Zare, R. N. HD ($v=1$, $j=2$, m) orientation controls HD–He rotationally inelastic scattering near 1 K. *J. Chem. Phys.* **150**, 174301 (2019).
31. Ketterle, W. & van Druten, N. J. Evaporative cooling of trapped atoms. *Adv. At. Mol. Opt. Phys.* **37**, 181–236 (1996).
32. Ni, K. K. et al. Dipolar collisions of polar molecules in the quantum regime. *Nature* **464**, 1324–1328 (2010).
33. Perreault, W. E., Mukherjee, N. & Zare, R. N. Stark-induced adiabatic Raman passage examined through the preparation of D_2 ($v=2$, $j=0$) and D_2 ($v=2$, $j=2$, $m=0$). *J. Chem. Phys.* **150**, 234201 (2019).
34. Mukherjee, N. & Zare, R. N. Stark-induced adiabatic Raman passage for preparing polarized molecules. *J. Chem. Phys.* **135**, 024201 (2011).
35. Mukherjee, N., Perreault, W. E. & Zare, R. N. in *Frontiers and Advances in Molecular Spectroscopy* (ed. Laane, J.) 1–46 (Elsevier, 2018).
36. Perreault, W. E., Zhou, H., Mukherjee, N. & Zare, R. N. Harnessing the power of adiabatic curve crossing to populate the highly vibrationally excited H_2 ($v=7$, $j=0$) level. *Phys. Rev. Lett.* **124**, 163202 (2020).
37. Mukherjee, N., Dong, W. & Zare, R. N. Coherent superposition of M-states in a single rovibrational level of H_2 by Stark-induced adiabatic Raman passage. *J. Chem. Phys.* **140**, 074201 (2014).
38. Croft, J. F. E., Balakrishnan, N., Huang, M. & Guo, H. Unraveling the stereodynamics of cold controlled HD–H_2 collisions. *Phys. Rev. Lett.* **121**, 113401 (2018).
39. Blatt, J. M. & Biedenharn, L. C. The angular distribution of scattering and reaction cross sections. *Rev. Mod. Phys.* **24**, 258–272 (1952).
40. Arthurs, A. M. & Dalgarno, A. The theory of scattering by a rigid rotator. *Proc. R. Soc. A* **256**, 540–551 (1960).
41. Diep, P. & Johnson, J. K. An accurate H_2–H_2 interaction potential from first principles. *J. Chem. Phys.* **112**, 4465–4473 (2000).
42. Buck, U. Rotationally inelastic scattering of hydrogen molecules and the non-spherical interaction. *Faraday Discuss. Chem. Soc.* **73**, 187–203 (1982).
43. Buck, U., Huisken, F., Kohlhase, A., Otten, D. & Schaefer, J. State resolved rotational excitation in D_2 + H_2 collisions. *J. Chem. Phys.* **78**, 4439–4450 (1983).
44. Chefdeville, S. et al. Appearance of low energy resonances in CO–*para*-H_2 inelastic collisions. *Phys. Rev. Lett.* **109**, 023201 (2012).
45. Hu, M. G. et al. Direct observation of ultracold bimolecular reactions. *Science* **366**, 1111–1115 (2019).

Methods

Pure D_2 gas (Cambridge Isotope Labs, 99.8%) at a stagnation pressure of 250 p.s.i. is supersonically expanded from an Even–Lavie pulsed valve[46] and collimated to form a molecular beam (divergence, 12 mrad) using a narrow (1 mm) skimmer placed at a distance of ~10 cm from the pulsed valve. The collimated beam defines the direction of the collision velocity in the lab frame. The bond axes of the D_2 molecules are aligned with respect to this axis, thus controlling the collision geometry at the molecular level. Using (2 + 1) REMPI, the rotational population distribution of the $v=0$ ground state of D_2 in the beam before state preparation was measured to be 38% in $j=0$, 36% in $j=1$, 24% in $j=2$ and 2% in $j=3$. Nearly all the $(v=0, j=0)$ molecules are pumped to the $(v=2, j=2)$ state[33], leaving primarily the $(v=0, j=1, 2)$ molecules as potential unprepared collision partners.

The D_2 $(v=0, j=0)$ molecules in the beam are transferred to the $(v=2, j=2, m)$ state using a coherent optical process called SARP. SARP accomplishes population transfer between a pair of rovibrational states using two-photon excitation with far-off resonant intermediate states. To transfer the complete population to a target state, SARP manipulates the crossings of the optically dressed adiabatic states using a pair of partially overlapping phase-coherent nanosecond laser pulses. The dynamic Stark shift from the intense laser pulses controls the crossing of resonance. The efficiency of adiabatic population transfer relies on a slow sweeping rate of the Stark-induced detuning and a strong two-photon Rabi frequency that lifts the degeneracy of the adiabatic states at the crossing. To transfer the complete population of D_2 $(v=0, j=0)$ to D_2 $(v=2, j=2, m)$ we used a strong Stokes pulse (10 ns, 1,064 nm, 100 J mm^{-2}) partially overlapping with a weaker pump pulse (5 ns, 655 nm, 20 J mm^{-2}) intersecting the molecular beam transversely. The Stokes pulse is obtained from an injection-seeded, Q-switched Nd^{3+}:YAG laser (PRO-290, Spectra-Physics), and the pump pulse is derived from a pulsed dye amplifier (PrecisionScan, Sirah) seeded by a frequency-stabilized ring dye laser (Matisse, Sirah) and pumped by the second harmonic of the pump laser. Following an optical delay of 6 ns, the pump and Stokes beams are combined using a dichroic beamsplitter before being focused onto the molecular beam using a 50 cm focal length lens. The region of the molecular beam excited by SARP is experimentally measured to have a diameter of ~100 μm. More detailed descriptions of SARP can be found elsewhere[33–36].

We can choose the bond axis alignment prepared by the SARP process by manipulating the polarizations of the laser pulses. The HSARP and VSARP alignments discussed in this work are prepared by polarizing both the optical fields of the pump and Stokes laser pulses either parallel (HSARP) or perpendicular (VSARP) to the molecular beam axis. In HSARP the bond axis of D_2 $(v=2, j=2)$ is preferentially aligned along the collision velocity, while for the VSARP state the bond axis is aligned perpendicularly. Choosing the quantization z axis along the collision velocity direction, the HSARP and VSARP states can be expressed as

$$|\mathrm{HSARP}\rangle = |j=2, m=0\rangle \text{ and}$$

$$|\mathrm{VSARP}\rangle = -\tfrac{1}{2}|j=2, m=0\rangle + \sqrt{\tfrac{3}{8}}\left(|j=2, m=2\rangle + |j=2, m=-2\rangle\right).$$

Both the SARP-prepared and scattered D_2 are probed using an ultraviolet laser pulse (5 ns, ~213 nm, 0.6 J mm^{-2}) that state selectively ionizes them by (2 + 1) REMPI. An ultraviolet beam collimator was designed to control the probe spot size on the molecular beam. The REMPI pulse is obtained by using two different β-barium borate crystals in sequence to generate the third harmonic of a tunable pulsed dye laser (Cobra-Stretch, Sirah) pumped by a Q-switched Nd^{3+}:YAG laser (PL9020, Continuum Lasers). The velocity distribution of the scattered molecules along the molecular beam axis is directly determined from the measured time-of-flight spectrum. Because the scattering centre-of-mass frame coincides with the moving frame of reference of the molecular beam, the scattering angular distribution can then be easily extracted from the velocity distribution[28]. The probe polarization is held perpendicular to the time-of-flight axis to minimize the contribution of photoelectron recoil velocity[47] to the measured time-of-flight spectrum.

To control the collision temperature, we probed the scattering at different delays between 50 and 600 ns following SARP preparation. For the D_2 molecules, which are travelling at the supersonic speed of ~2 km s^{-1}, these delays correspond to distances of 0.1 and 1.2 mm downstream from the SARP preparation site.

The scattering signal is maximized when the REMPI spot is centred on the moving volume of SARP molecules. This is because the rotationally relaxed D_2 $(v=2, j'=0)$ molecules, which move at ~800 m s^{-1} with respect to the molecular beam frame, are rapidly deflected out of the beam after they are produced. As a result, only those collisions that occur within the REMPI volume are detected. This has been experimentally verified by rastering the REMPI probe along the molecular beam.

Because the state preparation and detection take place within the narrow confines of the focused laser spots that last only for a few nanoseconds, the process works as a temporal gate selecting the narrow velocity group that is able to reach the probed volume in a given time. The velocity distribution of SARP-prepared D_2 is therefore squeezed within the small REMPI probe volume as the displacement along the molecular beam axis is increased. Because we only detect scattering products generated within the REMPI spot, this laser gating action reduces the collision temperature of the molecules contained in the probed volume.

Using (2 + 1) REMPI we recorded the velocity spectra of the SARP-prepared D_2 $(v=2, j=2)$ and unprepared D_2 $(v=0, j)$ molecules at each of the probe sites. The velocity spectra extracted from these measurements are given in Supplementary Information, section 1. These measurements were then used to calculate the collision velocity distribution between different D_2 collision pairs using the following equation:

$$f(v_c) = \int_{-\infty}^{\infty} \exp\left[-(x/\Delta_1)^2\right] \exp\left[-((x - v_0 + v_c)/\Delta_2)^2\right] \mathrm{d}x.$$

Here, Δ_1 and Δ_2 represent the width of the individual velocity distributions of the colliding pairs, and v_0 gives the difference in their peak speed. For collisions between excited pairs of D_2 molecules, $\Delta_1 = \Delta_2$. The collision speed distribution is given by $g(u_c) = f(u_c) + f(-u_c)$. The calculated collision speed distributions at 50 and 200 ns delays are displayed in Fig. 2d for various collision pairs. The collision speed u_{90} in Fig. 3, which gives the upper boundary that contains 90% of the collisions, is determined from the integral equation $\frac{\int_0^{u_{90}} g(u_c)\,\mathrm{d}u_c}{\int_0^{\infty} g(u_c)\,\mathrm{d}u_c} = 0.9$.

Data availability

Source data are provided with this paper.

References

46. Even, U. The Even–Lavie valve as a source for high intensity supersonic beam. *EPJ Tech. Instrum.* **2**, 17 (2015).
47. Perreault, W. E., Mukherjee, N. & Zare, R. N. Angular and internal state distributions of H_2^+ generated by (2 + 1) resonance enhanced multiphoton ionization of H_2 using time-of-flight mass spectrometry. *J. Chem. Phys.* **144**, 214201 (2016).

Acknowledgements

This work was supported by the US Army Research Office through the MURI programme under grant number W911NF-19-1-0283 and the National Science Foundation under grant number PHY- 2110256.

Author contributions

Experimental data were taken by H.Z., W.E.P. and N.M., and analysis and calculations were performed by N.M. All authors participated in discussion and writing of the manuscript.

Competing interests

The authors declare no competing interests.

Additional information

Supplementary information The online version contains supplementary material available at https://doi.org/10.1038/s41557-022-00926-z.

Correspondence and requests for materials should be addressed to Nandini Mukherjee or Richard N. Zare.

Peer review information *Nature Chemistry* thanks Roland Wester and the other, anonymous, reviewer(s) for their contribution to the peer review of this work.